water

MDPI

Article

Hydrogeochemical Characteristics of Hot Springs and Mud Volcanoes and Their Short-Term Seismic Precursor Anomalies Around the Muji Fault Zone, Northeastern Pamir Plateau

Shihan Cui [1], Fenna Zhang [2,3], Xiaocheng Zhou [1,4,*], Jingchao Li [1,*], Jiao Tian [1], Zhaojun Zeng [1], Yuwen Wang [1], Bingyu Yao [4], Gaoyuan Xing [1], Jinyuan Dong [1], Miao He [1], Han Yan [4], Ruibin Li [1], Wan Zheng [1], Kayimu Saimaiernaji [5], Chengguo Wang [5], Wei Yan [5] and Rong Ma [5]

1 United Laboratory of High-Pressure Physics and Earthquake Science, Institute of Earthquake Forecasting, China Earthquake Administration, Beijing 100036, China; c1416102468@163.com (S.C.); tianjiao375@163.com (J.T.); zzj00616@163.com (Z.Z.); wyw20010122@163.com (Y.W.); xinggy2219@163.com (G.X.); dongjinyuan@163.com (J.D.); iefhemiao@163.com (M.H.); 18319384995@163.com (R.L.); 13614377263@163.com (W.Z.)
2 Observation and Research Station of Tianjin Low-Medium Temperature Geothermal Resources, Tianjin Municipal Bureau of Planning and Natural Resources, Tianjin 300250, China; ying-ying22@163.com
3 Tianjin Geothermal Exploration and Development-Designing Institute, Tianjin 300250, China
4 School of Earth Sciences and Resources, China University of Geosciences, Beijing 100083, China; yaobingyu2022@163.com (B.Y.); 16631157365@163.com (H.Y.)
5 Earthquake Agency of Xinjiang Uygur Autonomous Region, Urumqi 830011, China; samar861226@163.com (K.S.); 15709918384@163.com (C.W.); yanwei.nan@163.com (W.Y.); mrxjeq@126.com (R.M.)
* Correspondence: zhouxiaocheng188@163.com (X.Z.); lijc@ief.ac.cn (J.L.)

Abstract

The Muji Fault Zone (MJF) in the northeastern Pamir Plateau hosts a well-developed non-volcanic geothermal system, characterized by widespread hot springs and mud volcanoes—where core processes of geothermal fluids, including atmospheric precipitation recharge, shallow crustal circulation, carbonate-driven water–rock interactions, and CO_2-rich fluid discharge, are tightly coupled with regional intense crustal deformation and frequent seismic activity. We collected and analyzed 22 geothermal water samples and 8 bubbling gas samples from the MJF periphery, finding that the geothermal waters are predominantly of the HCO_3-Ca·Mg hydrochemical type, with hydrogen (δD: −103.82‰ to −70.21‰) and oxygen ($\delta^{18}O$: −14.89‰ to −10.10‰) isotopes indicating atmospheric precipitation as the main recharge source. The Na-K-Mg ternary diagram classified the waters as immature, reflecting low-temperature water–rock interactions in the shallow crust (<3 km), while noble gas isotopes ($^3He/^4He$: 0.03–0.09 Ra, Ra = 1.43×10^{-6}) and carbon isotopes ($\delta^{13}C$-CO_2) confirmed fluid origin from crustal carbonate dissolution; SiO_2 geothermometry estimated thermal reservoir temperatures at 67–155 °C. Long-term monitoring (May 2019–April 2024) of Tahman (THM) and Bulake (BLK) springs revealed significant pre-seismic anomalies: before the 2023 Tajikistan *Ms*7.2 and 2024 Wushi *Ms*7.1 earthquakes, Na^+, Cl^-, and SO_4^{2-} concentrations showed notable negative anomalies (exceeding 2σ of background values) with synchronous trends between the two springs. Integrating these findings, a "Fault-Spring-Mud Volcano-Earthquake" fluid response model was established, providing direct evidence of deep-shallow fluid coupling in mud volcano–geothermal fluid interactions. This study enhances understanding of the dynamic evolution of non-volcanic geothermal systems under tectonic stress and clarifies the mechanisms of hydrogeochemical variations in fault-controlled geothermal systems, offering a robust scientific basis for advancing research on tectonic–fluid interactions in active fault zones of the northeastern Pamir Plateau.

Academic Editor: Achim A. Beylich

Received: 16 September 2025
Revised: 3 November 2025
Accepted: 10 November 2025
Published: 13 November 2025

Citation: Cui, S.; Zhang, F.; Zhou, X.; Li, J.; Tian, J.; Zeng, Z.; Wang, Y.; Yao, B.; Xing, G.; Dong, J.; et al. Hydrogeochemical Characteristics of Hot Springs and Mud Volcanoes and Their Short-Term Seismic Precursor Anomalies Around the Muji Fault Zone, Northeastern Pamir Plateau. *Water* **2025**, *17*, 3241. https://doi.org/10.3390/w17223241

Keywords: mud volcano; hot spring; water-rock reaction; seismicity; Muji Fault; Pamir syntax; earthquake chemical precursors

1. Introduction

Geothermal fluids, serving as sensitive indicators of deep tectonic activities, carry critical information on water–rock interactions, volatile migration, and energy transfer processes, providing direct evidence for studying the dynamic mechanisms of active fault zones [1–3]. During seismic preparation, variations in fluid pressure, porosity adjustments driven by mineral phase transitions, and dynamic permeability evolution within fault zones [4,5] significantly alter the chemical composition, gas composition, and isotopic signatures of geothermal waters [6–9]. Continuous geochemical monitoring can thus delineate deep fluid migration pathways and material sources while revealing porosity variations in underlying rock layers [10–12]. Particularly in seismically active regions such as fault intersections, structural changes in fractures may trigger rapid physicochemical responses in fluids, offering observable surface signals for understanding earthquake nucleation mechanisms and short-term precursor identification [13].

The northeastern Pamir Plateau, located at the convergent margin of the northwestern Tibetan Plateau and the Indo-Asian subduction front, is a natural laboratory for studying fluid–tectonic interactions due to its intense tectonic activity [14,15]. This region hosts several major fault systems, including the MJF, which provide critical conduits for geothermal fluid circulation and give rise to diverse geothermal manifestations [16–19]. Consequently, a series of hydrogeochemical studies have provided fundamental insights into the regional geothermal background. For instance, research by Li et al. in the Tashkurgan Basin revealed a high-temperature geothermal system characterized by Cl·SO_4-Na type waters, formed through water–rock interaction with reservoir temperatures reaching 250–260 °C [18]. These waters are recharged by local precipitation and glacial meltwater and mix with shallow groundwater during ascent, with permeable pathways formed by the intersection of NNW- and NE-trending fault sets. Chelnokov et al. proposed that CO_2-rich springs in the Pamir are Ca-HCO_3 type waters, resulting from the mixing of mantle-derived volatiles ascending along faults with cold water [16]. Furthermore, Chen et al. identified a high-temperature (up to 260.96 °C), shallow–deep mixed reservoir geothermal system of the Cl·SO_4-Na type in the northeastern Pamir [17]. Its genesis is attributed to meteoric water infiltrating along deep faults, mixing with magmatic fluids, and being heated by multiple sources (magmatic, radiogenic, and frictional heat) to form a parent fluid that undergoes adiabatic cooling during ascent, a process supported by elevated B, Li, and Cl concentrations indicative of magmatic input [17].

However, previous studies have largely concentrated on the macroscopic features of regional-scale geothermal systems [15,19,20]. They have seldom focused on the fine-grained hydrogeochemical processes of specific fault systems, lacking detailed investigation into trace element evolution and long-term dynamic monitoring. Critically, these studies have not integrated fluid geochemical dynamics with the activity and seismogenic processes of specific faults. The recent occurrence of the 2023 *Ms*7.2 Tajikistan and 2024 *Ms*7.1 Wushi earthquakes near the study area provides a unique opportunity to investigate fluid geochemical precursor anomalies in a specific tectonic context, highlighting the urgency and importance of focusing on key fault zones.

The MJF, with its unique tectonic setting and geological phenomena, presents an ideal window to respond to these seismic events and address the aforementioned research gaps. This active fault zone not only hosts mud volcanoes but also intersects with the

Kongur Extension System to form a dense fracture network [15,20,21]. This creates complex pathways for the upwelling of deep fluids and their interaction with shallow groundwater, making the system potentially highly sensitive to changes in crustal stress [17,22]. This makes it an ideal site to investigate seismic responses in geothermal fluid-mud volcano systems. Therefore, this study collected and analyzed 22 geothermal water samples from the periphery of the MJF and 8 gas samples from the Muji mud volcano. Major/trace element data, hydrogen-oxygen isotopes, and carbon/rare gas isotopes were obtained. Long-term hydrochemical monitoring was conducted on the Bulake (BLK) within the MJF and the typical geothermal spring Tahman (THM) in the Tashkurgan Basin [23]. By systematically analyzing geothermal water and mud volcano gas samples from its periphery, combined with long-term monitoring data from key sites, we aim to delineate its detailed geochemical characteristics and capture fluid-related pre-seismic responses. Ultimately, this research will establish an integrated "fault-spring-mud volcano-earthquake" fluid response model. We expect this work to refine insights into tectonic–fluid interactions in active fault zones from a novel fluid geochemical perspective and contribute to advancing research on geothermal system dynamics.

2. Geological Setting

Pamirs Plateau, located at the western syntaxis of the Himalayan-Tibetan orogenic belt, represents one of the most tectonically active regions on Earth. This high-elevation plateau is a critical zone for studying continental collision dynamics, lithospheric deformation, and deep mantle processes associated with the ongoing convergence between the Indian and Eurasian plates [24,25].

The northeastern margin lies within the West Kunlun-Karakoram orogenic belt, bounded by the Kongur Shan extensional system (KSES) to the west and the Pamir Frontal Thrust (PFT) to the east [26]. Major fault systems, including the MJF, Tashkurgan Fault (TKF), and Kangwa Fault (KWF), dominate the region's structural architecture, facilitating both crustal thickening and extensional basin development [23,27].

Among these structures, MJF is particularly prominent for its pivotal role in shaping the Quaternary geology and geothermal systems of the Muji Basin [28–30]. It is a Holocene-active, right-lateral strike-slip fault with a thrust component, trending NW-SE for approximately 20 km and dipping to the northeast at 50–65°. Its neotectonic activity, characterized by southwestern compressional thrusting and right-lateral displacement, not only governs regional groundwater circulation, the upwelling of CO_2-rich geothermal fluids, and the deposition of laminated travertines, but also involves interaction with the adjacent Southern Fault of the Kungai Mountains (SFKM) to form an extensional system, promoting basin subsidence and fluid migration [31]. Geophysical data indicate that the MJF roots into mid-crustal ductile shear zones, linking surface deformation to deeper crustal processes, and its proximity to the high heat flow region of the Pamir (70–90 $mW \cdot m^{-2}$) further enhances its function in localizing geothermal activity [17]. The entire fault system is driven by the north–south compressive stress field of the Pamir Plateau, and its significant seismic potential was underscored by the 2016 *Ms*6.7 Aketao earthquake [32]. This seismic event not only confirmed the fault's activity but also promoted the development of secondary fractures, providing additional conduits for geothermal fluids to ascend to the surface.

3. Sampling and Methods

From April 12th to 18th, 2023, 22 geothermal water samples, 8 gas samples, snow water samples (s23, s24), and river water samples from the upper, middle, and lower reaches (s25–s27) were collected in and around the MJF for background analysis. The sampling locations are shown in Figure 1 and Table 1, photographs of representative locations around

the MJF are shown in Figure 2. The main information of the geothermal water samples and the compositional characteristics of the gas samples are presented in Table S1 and Table 2, respectively.

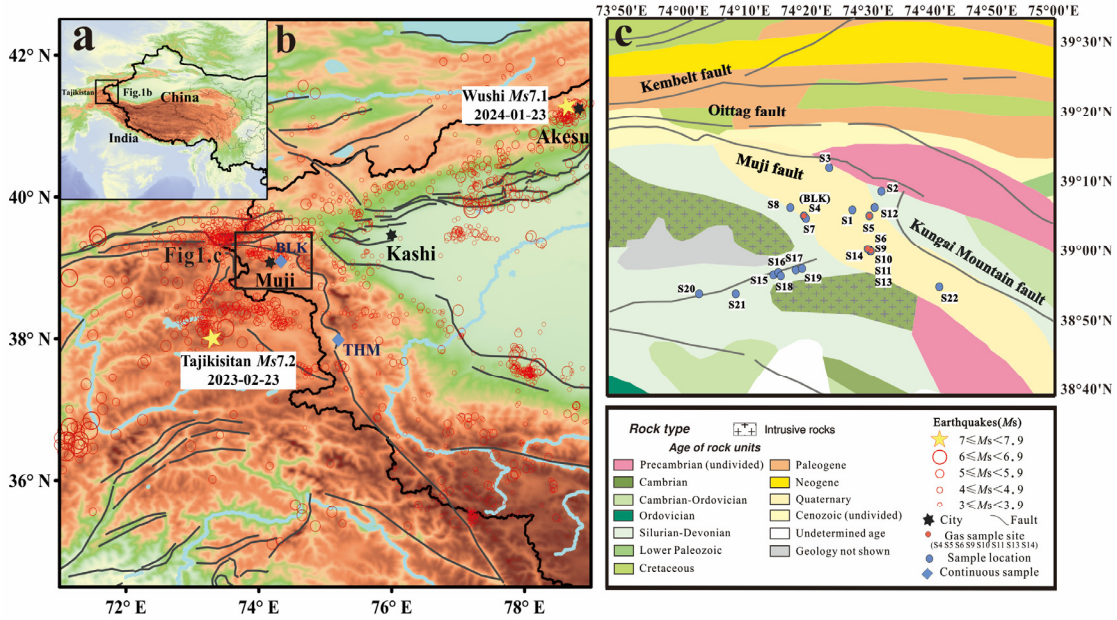

Figure 1. The plot of sampling site distribution; (**a**) Localization of the area of this study; (**b**) Terrain and earthquake distribution in the Muji fault area; (**c**) Simplified Geological Scheme in the MJF (Geological data is sourced from Steinshouer et al. [33]).

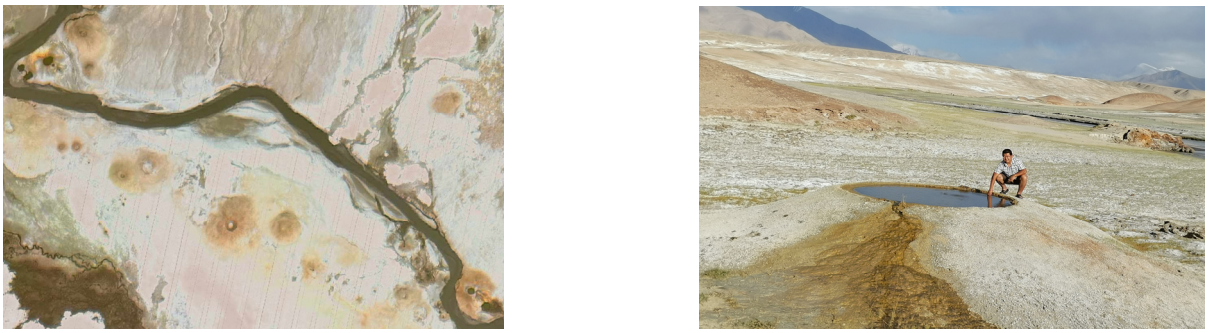

Figure 2. Photographs of representative locations around the MJF.

Table 1. Location of the surveyed area of hot spring in the MJF.

No.	Site	Longitude	Latitude	Altitude
S1	Bulake Spring 1	74.4583	39.1033	3524.51
S2	Mining Area Spring	74.5436	39.1378	3714.62
S3	Bulake Spring 2	74.4092	39.2103	4020.47
S4 (BLK)	Bulake Village Spring	74.3253	39.1044	3523.78
S5	Muji River Spring 1	74.5089	39.0189	3447.81
S6	Muji River Spring 2	74.5019	39.0175	3458.14
S7	Border Defense Highway Spring	74.3453	39.0667	3521.72
S8	Bridge—Under Spring	74.2834	39.1144	3541.76
S9	Muji River Spring 3	74.5056	39.0003	3542.65
S10	Muji River Spring 4	74.5233	38.9981	3449.73
S11	Muji River Spring 5	74.5106	38.9989	3451.57
S12	Mud Volcano	74.5383	39.1156	3448.79

Table 1. *Cont.*

No.	Site	Longitude	Latitude	Altitude
S13	Muji River Spring 6	74.5214	39.1158	3450.81
S14	Muji River Spring 7	74.4981	39.0003	3468.80
S15	Qiongrang Village Spring 1	74.2419	38.9439	3593.09
S16	Qiongrang Village Spring 2	74.2678	38.9497	3587.50
S17	Qiongrang Village Spring 3	74.3097	38.9503	3560.15
S18	Qiongrang Village Spring 4	74.2669	38.9378	3590.24
S19	Qiongrang Village Spring 5	74.3433	38.9706	3551.90
S20	Qiate	74.0756	38.8908	3846.30
S21	Winter Pasture	74.1431	39.0936	4072.64
S22	Kuntibiesi Village	74.6975	38.9001	3419.87
S23	Upstream Snowmelt Water	75.0153	40.4547	3541.74
S24	Midstream Snowmelt Water	73.9006	39.7658	2988.93
S25	Upstream River Water	74.0919	39.7706	2699.03
S26	Midstream River Water	74.3542	39.8433	2478.96
S27	Downstream River Water	74.4544	39.9706	2699.73

Table 2. The data of Hot spring gases composition and helium isotope in the MJF.

Sample	R/Ra	$^{3}He/^{4}He(R)$	He (ppm)	$^{4}He/^{20}Ne$	Ar%	H_2 (ppm)	CO_2 (%)	N_2 (%)	O_2 (%)	CH_4 (%)	$^{4}He/^{20}Ne$
S4	0.03	4.26×10^{-8}	394	205	0.16	2.4	74.80	24.409	0.0257	0.0399	205
S5	0.06	8.93×10^{-8}	32	64	0.062	1	94.60	4.8465	0.0442	0.0439	64
S6	0.07	9.73×10^{-8}	171	142	0.17	1.1	85.50	13.635	0.0408	0.0544	142
S9	0.09	1.23×10^{-7}	116	90	0.052	1	94.70	4.3602	0.0424	0.0422	90
S10	0.07	9.67×10^{-8}	56	222	0.035	0.9	96.90	2.5515	0.0676	0.0048	222
S11	0.07	9.11×10^{-8}	41	162	0.057	1.2	96.60	3.052	0.2467	0.048	162
S13	0.09	1.32×10^{-7}	297	53	0.3	1.1	73.80	25.468	0.032	0.0062	53
S14	0.06	7.88×10^{-8}	157	120	0.11	1.1	90.80	8.781	0.0304	0.007	120

3.1. Collection and Analysis of Geothermal Water Samples

Twenty-two geothermal spring samples were collected to analyze major/trace elements, stable isotopes (δD, $\delta^{18}O$), dissolved silica, and inorganic carbon species. Samples were collected using 250 mL acid-washed polyethylene bottles, triple-rinsed with deionized water to eliminate air contamination. Field measurements included temperature recorded using a precision YF-16 digital thermometer (accuracy ±0.1 °C). To maintain the stability of trace elements, 1–2 drops of 14 M nitric acid were added, adjusting the pH to below 2. Each analytical batch was preceded by instrument calibration using certified standards (chromatographic accuracy ±0.2‰). Ionic constituents (K^+, Na^+, Mg^{2+}, Ca^{2+}, F^-, Cl^-, NO_3^-, SO_4^{2-}) were quantified via an ion chromatograph (Thermo Scientific Dionex AQUION IC, Thermo Fisher Scientific, Waltham, MA, USA) equipped with an AS40 automatic sampler.

Carbonate alkalinity was measured via potentiometric titration using a ZDJ-100 titrator with 0.05 M HCl (reproducibility ±2%). Trace elements (Li, B, Al, Ba, Ge, Rb, Cs, V, Be, Mo, Cr, Sr, and Sb) were analyzed using an Agilent 8900 ICP-QQQ (Agilent Technologies, Santa Clara, CA, USA). The analytical precision, expressed as the relative standard deviation (RSD), was within 5% [34]. Oxygen ($\delta^{18}O$) and hydrogen (δD) isotopes were analyzed using a Picarro L2140-I liquid water and vapor isotope analyzer (Picarro Inc., Santa Clara, CA, USA), referenced to Vienna Standard Mean Ocean Water (V-SMOW). National reference standards (GBW04458, 04459, 04460 [35]) were used, with analytical precision of $\delta D < \pm 0.05‰$ and $\delta^{18}O < \pm 0.015‰$. Silica concentrations were measured via Optima-5300 DV ICP-OES (PerkinElmer Inc., Waltham, MA, USA) [36]. For DIC isotope analysis, 50 µg carbon aliquots were He-purged to remove atmospheric CO_2, reacted with 85% H_3PO_4 in Labco Exetainer® vials. After 24 h equilibration, evolved CO_2 was purified

and analyzed on a Picarro G2201-I against NBS-18 standard [37]. National reference standards (GBW04458, 04459, 04460) were employed, with analytical precision of $\delta D < \pm 0.05‰$ and $\delta^{18}O < \pm 0.015‰$. The analysis of $\delta^{13}C$ in dissolved inorganic carbon ($\delta^{13}C$ DIC) was conducted using a closed-system method. Water samples containing no less than 50 μg of carbon were purged with helium to eliminate residual CO_2, and then transferred into pre-evacuated Labco Exetainer tubes that had been flushed with helium (Labco Limited, Lampeter, UK). One milliliter of 85% phosphoric acid was injected into each tube, and the reaction was performed under sealed conditions to avoid isotopic exchange with atmospheric CO_2 [38]. Following a 24 h reaction period, the generated CO_2 was extracted, purified, and analyzed by a Picarro G2201-I Carbon Isotope Analyzer (Picarro Inc., Santa Clara, CA, USA), using the international standard NBS-18 as a reference. The overall analytical uncertainty was less than 0.1‰. The charge balance error was within ±10%, guaranteeing the reliability of major ion data [39]. The ion balance (ib) was calculated as follows:

$$ib[\%] = \frac{\sum cations - \sum anions}{(\sum cations + \sum anions)} \times 100$$

where acceptable analytical precision requires $|ib| < 5\%$ [40].

3.2. Collection and Analysis of Geothermal Gas Samples

Gas samples were gathered by the upward air venting method so as to minimize contamination. A glass bottle was attached to a funnel and filled with spring water to remove air bubbles. The bottle was afterward inverted, which allowed hot spring gases to displace the water completely. Once the bottle was full, the funnel was detached under water, and the bottle was sealed to prevent leakage or contamination. Gas samples were subjected to analysis at the Lanzhou Oil and Gas Resources Research Center, Chinese Academy of Sciences, focusing on three aspects: gas composition, helium isotope ratios ($^3He/^4He$ and $^4He/^{20}He$), and $\delta^{13}C$ in CO_2 ($\delta^{13}C$ CO_2).

Gas composition was measured with a MAT 271 mass spectrometer (Thermo Fisher Scientific, Bremen, Germany), with a relative standard deviation (RSD) of < 5%.$\delta^{13}C$ was analyzed using a gas chromatograph (Agilent 6890) connected with a Thermo Fisher Scientific Delta Plus XP stable isotope ratio mass spectrometer (Thermo Fisher Scientific, Bremen, Germany). $\delta^{13}C$ values were reported relative to the Vienna Pee Dee Belemnite (PDB) standard, and the measurement error was ±0.2‰. For helium isotope analysis, a two-stage separation and purification process was first applied to He and Ne, and then a Noblesse rare gas isotope mass spectrometer was utilized for the analysis [41]. Both $^3He/^4He$ and $^4He/^{20}Ne$ were measured in static mode, calibrated to the air standard, and the analytical error was ±3% [42].

4. Results

The detailed hydrogeochemical compositions and hydrogen-oxygen isotopic compositions of the studied hot springs are listed in Table S1. The measured temperatures of geothermal water at the sampling sites range from 0.9 to 14.9 °C, with the overall water temperature remaining below 25 °C, thus classifying these springs as cold springs. Cold springs are characterized by shallow circulation depths, indicating limited groundwater flow. The pH values of the water samples range from 6.54 to 9.61, approaching neutral conditions. The electrical conductivity of the water samples exhibits significant variability, ranging from 108.40 to 2431.00 μs/cm. Total dissolved solids (TDS) concentrations in the geothermal water vary between 60 and 2430 mg/L, indicating an overall low TDS level. The primary cations are Na^+ (5.55~144.22 mg/L), Ca^{2+} (7.04~434.26 mg/L), and Mg^{2+} (0.71~112.71 mg/L), while the main anion is HCO_3^- (39.52~1807.23 mg/L). In the study

area, Na^+, Ca^{2+}, and Mg^{2+} are the dominant cations, with HCO_3^- as the primary anion. The $\delta^{18}O$ and δD values of the samples vary in the ranges of −10.10 to −14.89‰ and −70.21 to −103.82‰, respectively. The hydrogeochemical and isotopic compositions of the hot spring gases are shown in Table 2. The trace gas components at the sampling points include Ar and He, with volume contents of 0.035–0.30% and 32–394 ppm, respectively. The $^3He/^4He$ ratios of the sampling points range from 4.26×10^{-8} to 1.32×10^{-7}, equivalent to 0.03–0.09 Ra (where Ra is the $^3He/^4He$ ratio in air, 1.43×10^{-6}), and the $^4He/^{20}Ne$ ratios range from 53 to 222-values higher than the atmospheric characteristic value of 0.318 [43].

5. Discussion

5.1. Water Chemistry and Water Isotope Characteristics

5.1.1. Origin of Major Elements in Hot Springs

The hydrochemical characteristics of the hot springs in the study area unequivocally point to a single dominant process: the dissolution of carbonate rocks. The Piper diagram (Figure 3) shows that all water samples are of the HCO_3-Ca-Mg type, a signature corresponding to the high concentrations of Ca^{2+} and Mg^{2+}, which are the direct products of calcite (Reaction 1) and dolomite (Reaction 2) dissolution [44–46]:

$$CaCO_3 + CO_2 + H_2O \rightarrow Ca^{2+} + 2HCO_3^- \quad (1)$$

$$CaMg(CO_3)_2 + 2CO_2 + 2H_2O \rightarrow Ca^{2+} + Mg^{2+} + 4HCO_3^- \quad (2)$$

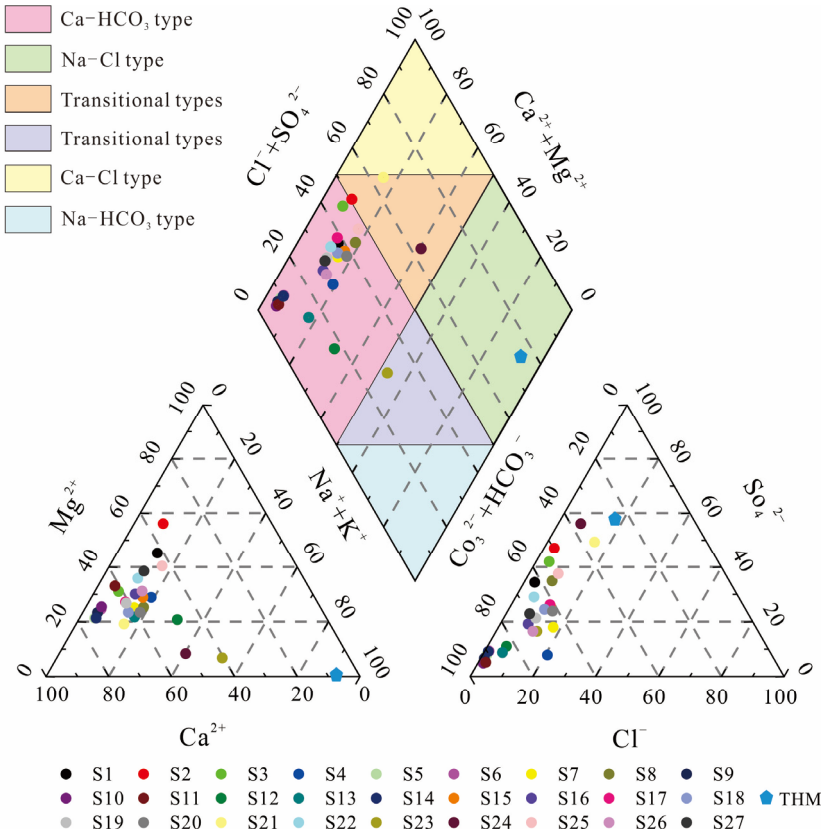

Figure 3. Piper diagram of samples in the MJF and THM [23].

This assertion is strongly supported by multiple lines of geochemical evidence. Key ionic ratios first reveal the relative contributions of different geochemical processes: the low Na^+/HCO_3^- ratio (<1, Figure 4) confirms that HCO_3^- is primarily derived from carbonate minerals rather than silicate weathering. Meanwhile, the significant positive correlation among Ca^{2+}, Mg^{2+}, and HCO_{3-} (Figure 5)—coupled with their weak cor-

relation with Cl^-—indicates that Ca^{2+} and Mg^{2+} originate from carbonate rock strata. Further, the sample points cluster distinctly near the carbonate weathering end-member on the logarithmic plot of Ca^{2+}/Na^+ versus $HCO_{3\_}/Na^+$ (Figure 6), further corroborating $HCO_{3\_}$'s dominant role.The CO_2 that drives the aforementioned carbonate dissolution reactions is likely derived from a dual source: infiltrating meteoric water and input from deep tectonic or magmatic activity [47]. Although carbonate dissolution is the dominant process, the low concentrations of Na^+ and K^+ in the water also suggest a subordinate role for silicate mineral (e.g., plagioclase) weathering (Reactions 3–4) [48]; however, its contribution to the overall water chemistry is evidently limited. The low Na^+ and K^+ concentrations, evidenced by trace cation signatures, may reflect localized plagioclase alteration (Reaction 3–4);

$$2NaAlSi_3O_8 + 3H_2O + 2CO_2 \rightarrow Al_2(Si_2O_5)(OH)_4 + 4SiO_2 + 2Na^+ + 2HCO_3^- \quad (3)$$

$$2KAlSi_3O_8 + 3H_2O + 2CO_2 \rightarrow Al_2(Si_2O_5)(OH)_4 + 4SiO_2 + 2K^+ + 2HCO_3^- \quad (4)$$

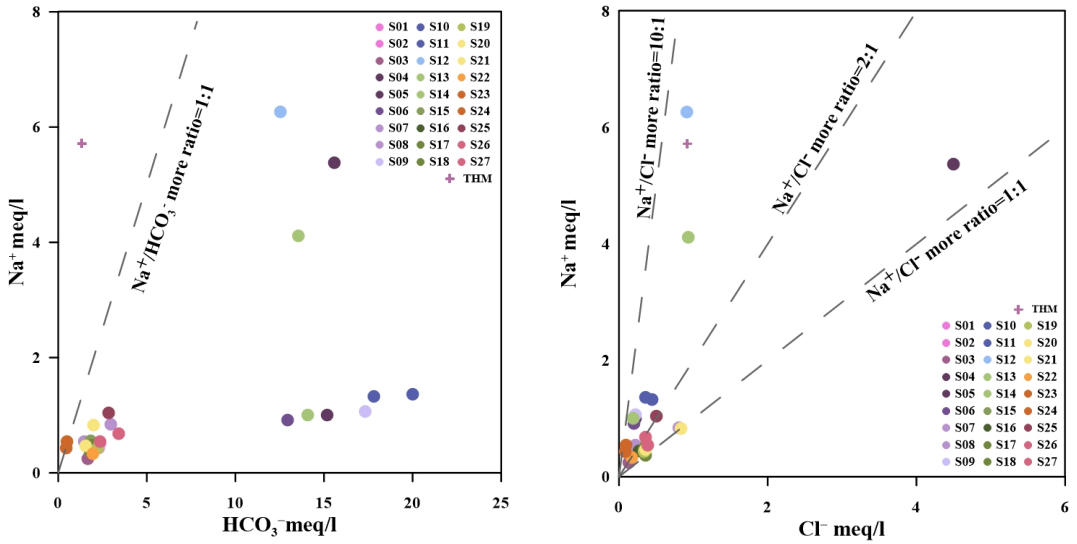

Figure 4. Na^+ versus HCO_3^- and Cl^- Ratio diagram of major ions in water sample.

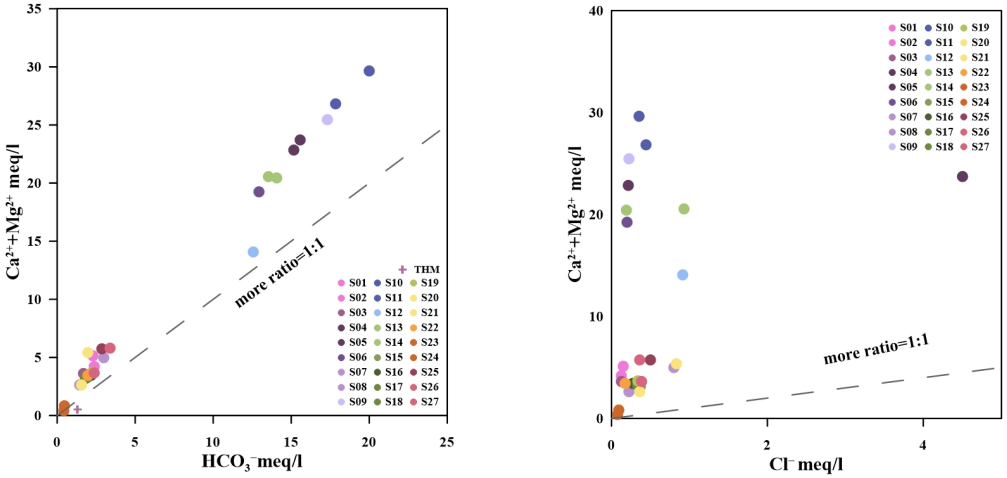

Figure 5. Ca^{2+}, Mg^{2+} versus HCO_3^- and Cl^- ratio diagram of major ions in water sample.

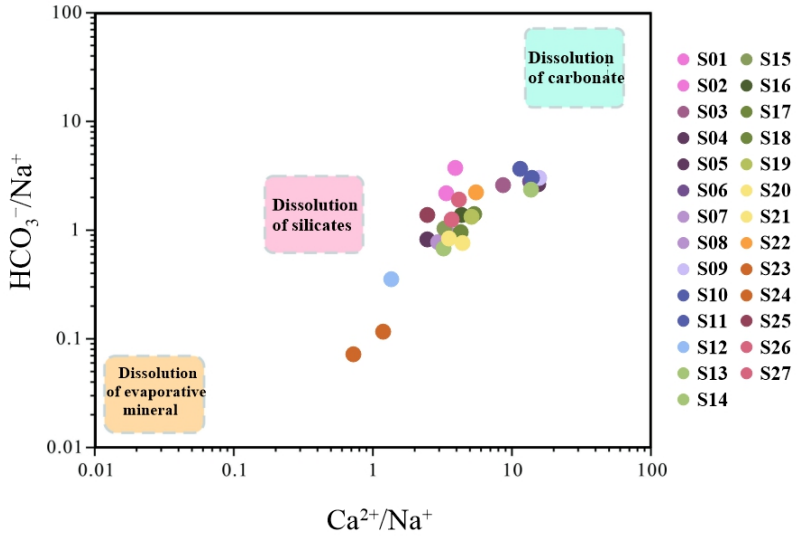

Figure 6. Scatter logarithmic plots of Ca^{2+}/Na^+ versus HCO_3^-/Na^+ illustrating the influence of mineral dissolution and weathering in groundwater.

5.1.2. Stable Oxygen and Hydrogen Isotopes

Stable hydrogen and oxygen isotope analysis provides further insights into the recharge source and circulation pathways of the hot springs. As shown in Figure 7, all water samples plot near the Global Meteoric Water Line (GMWL: $\delta D = 8\delta^{18}O + 10$) [49], clearly indicating a meteoric origin [50–54]. The slight deviation of the samples to the right of the GMWL, coupled with an insignificant $\delta^{18}O$ shift, suggests that evaporation effects were limited during deep circulation, while minor water–rock interaction or mixing of different water sources may have occurred [55]. More importantly, the samples exhibit a scattered distribution along the meteoric water line, which primarily reflects the isotopic "altitude effect"—the principle that precipitation from different elevations possesses distinct isotopic signatures [18,56].

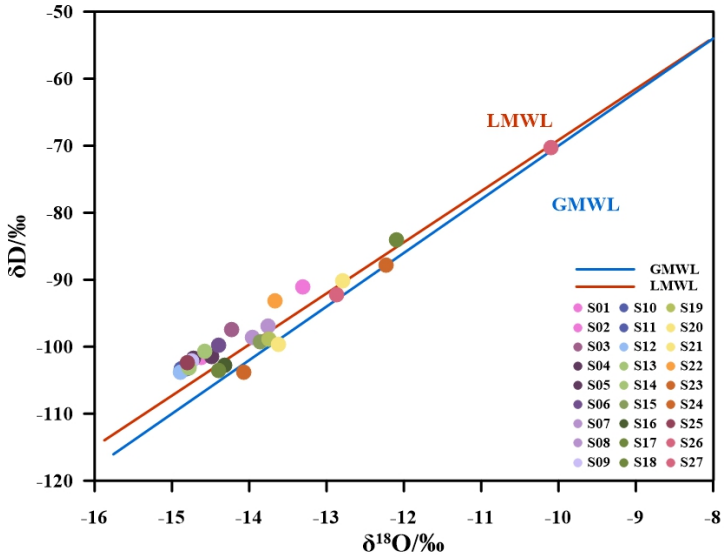

Figure 7. δD versus $\delta^{18}O$ values of water samples from the Muji fault area. GMWL [49]; LMWL: Local Meteoric Water Line [18].

5.1.3. Origin of Trace Elements in Hot Springs

The average trace element concentrations from 27 rock samples were adopted as reference values [57]. Nickel (Ni), a stable element ubiquitously present in the crust, was

selected as the reference element for calculating enrichment factors (EF_i). Seventeen trace elements were analyzed [58], with those below the detection limit (0.002 μg/L) excluded from the dataset. The enrichment factor was calculated using the formula:

$$EF_i = (C_i/N_i)_w/(C_i/N_i)_r$$

where N_i denotes the reference element concentration, C_i represents the trace element concentration, subscript water refers to hot spring water, and subscript rock refers to host rock.

Enrichment factor analysis ($EF_i < 1$) or trace elements in the MJF geothermal springs (Figure 8) indicates that their geochemical signatures are predominantly controlled by crustal rock weathering processes, with negligible contributions from deep hydrothermal inputs or anthropogenic sources [59], only the Sc element shows obvious enrichment characteristics different from other elements, which is considered to be caused by water–rock reaction between gabbro and diabase in this area [60]. This conclusion is further supported by the absence of characteristic hydrothermal element enrichments (e.g., Li, As, Rb) in the EF_i patterns [61].

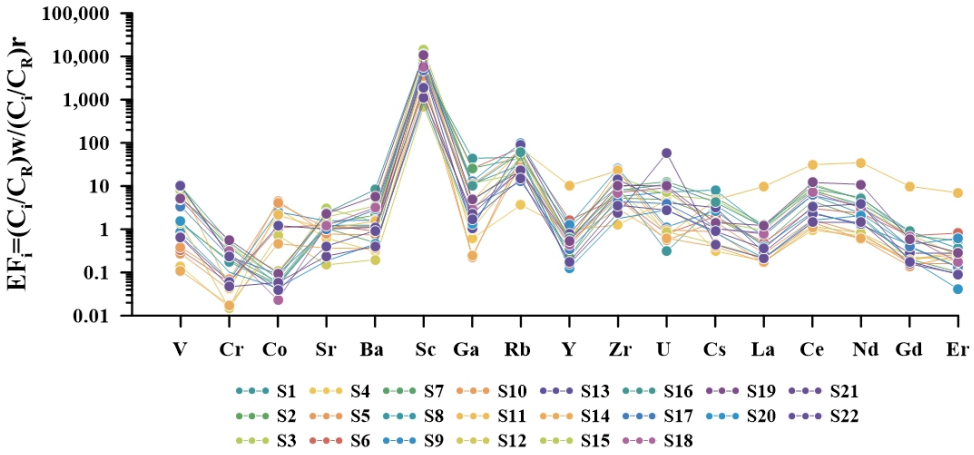

Figure 8. Diagram illustrating enrichment factors of trace elements (reference element is Ni).

5.1.4. Mineral Saturation States

The saturation index (SI) serves as a key parameter to characterize whether geothermal water is saturated or undersaturated with respect to specific minerals during fluid circulation. In this study, PHREEQC (version 2) software was used to calculate the SI of all hot spring water samples at in situ temperature and pH conditions [62]. The results (Figure 9) show that most springs (except S7) exhibit consistent SI patterns across different minerals. Supersaturation with carbonate minerals (e.g., calcite, dolomite; SI > 0) indicates potential precipitation of these minerals, reflecting intense interaction between groundwater and carbonate rocks (e.g., limestone, dolomite).

Hydrogeochemical evolution processes: During deep circulation, high-temperature groundwater dissolves carbonate (calcite, dolomite) and silicate minerals, releasing Ca^{2+}, Mg^{2+}, HCO_3^-, and dissolved SiO_2. As the fluid ascends to the surface, pressure decrease triggers CO_2 degassing, shifting the system toward supersaturation and promoting calcite/dolomite precipitation [48]. Concurrently, cooling reduces silica solubility, leading to quartz/chalcedony supersaturation [47].

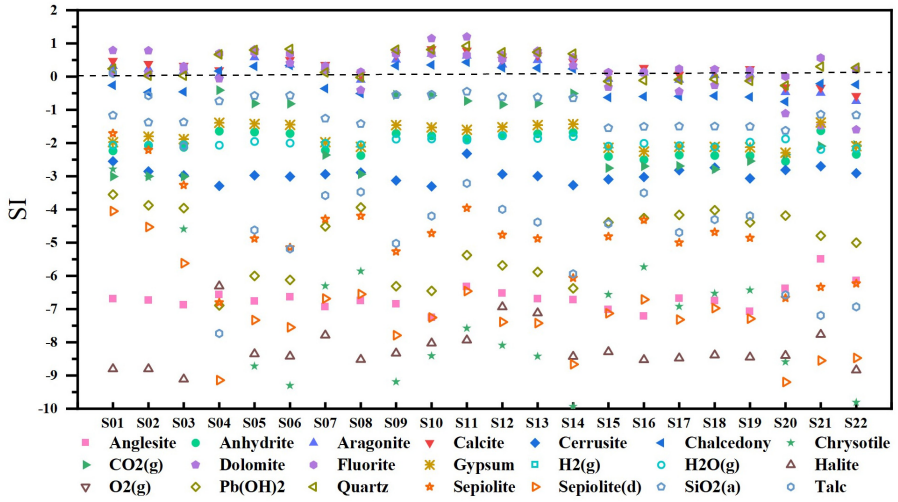

Figure 9. SI values of groundwater samples with respect to minerals.

5.2. Reservoir Temperature

Estimating reservoir temperature is key to understanding the potential of a geothermal system [47,63,64]. However, reliable temperature estimation depends on selecting an appropriate geothermometer. The Na-K-Mg ternary diagram (Figure 10) shows that all water samples in the Muji fault plot in the 'immature waters' field, indicating that the waters have mixed with shallow cold water during ascent and are far from reaching full chemical equilibrium with the host rock [47]. THM's classification within the "partially equilibrated" zone is now attributed to deeper circulation pathways influenced by basin-scale faults, contrasting with the immature waters dominant within the MJF [23]. Mineral saturation indices (Figure 9) corroborate this finding, showing that most minerals, with the exception of a few species, are in an undersaturated state. This prevalent state of non-equilibrium and immaturity renders the results from cation geothermometers (e.g., Na-K, K-Mg), which depend on water–rock equilibrium, unreliable.

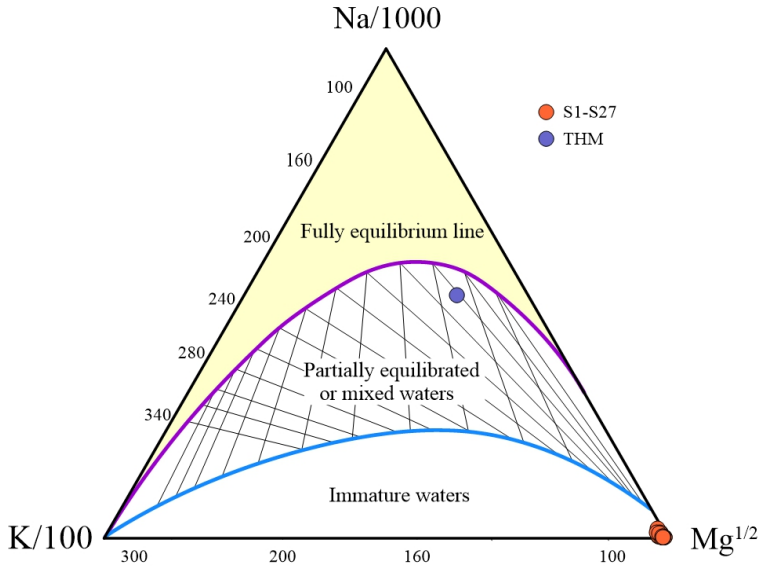

Figure 10. Saturation indices values of groundwater samples with respect to minerals.

Therefore, we selected the SiO_2 geothermometer [63,64], which relies on the dissolution/precipitation equilibrium of quartz or its polymorphs. It is suitable for geothermal systems like the one in this study, which are characterized by relatively low reservoir temperatures (<250 °C) and chemically immature waters [47,64].

The depth was calculated using the formula:

$$H = \frac{T - T_0}{g} + h$$

The average temperature in the study area is taken as 3.3 °C, the geothermal temperature gradient is 5.59 °C/100 m, and the depth of the normothermic zone is 20 m [65].

As seen in Table 3, this method yields an estimated reservoir temperature range for the study area of 67 to 155 °C and circulation depths of 1143 to 2738 m.

Table 3. Calculation of reservoir temperature and circulation depth using geothermometers.

Sample	SiO_2 (mg/L)	Quartz Thermometer Scale 1 (°C)	Circulation Depth (m)
S1	5.7	102	1788
S2	22.2	152	2681
S3	3.6	86	1501
S4	13.2	132	2325
S5	19.7	148	2600
S6	19.4	147	2588
S7	4.1	91	1583
S8	2.8	78	1349
S9	23.9	155	2734
S10	23.4	154	2721
S11	23.6	155	2727
S12	3.0	80	1394
S13	20.7	149	2634
S14	20.1	148	2615
S15	2.0	67	1153
S16	2.7	77	1335
S17	2.3	70	1221
S18	2.5	74	1280
S19	2.0	67	1151
S20	2.0	66	1140
S21	5.8	102	1795
S22	4.7	95	1667
S23			
S24	-	-	
S25	-	-	
S26	-	-	
S27	-	-	

5.3. Geochemical Characteristics of Hot Spring Gas

5.3.1. The Source of Helium

The helium isotope systematics of the associated hot spring gases provide direct evidence for constraining the fluid sources [42,66,67]. The measured $^3He/^4He$ ratios (0.01–0.05 Ra) in this study consistently fall within the typical crustal range (Figure 11), unequivocally indicating a predominantly crustal origin with negligible helium input from the mantle [68]. This conclusion is highly consistent with the other geochemical characteristics of the integrated water-gas system, which are discussed collectively below with the origin of CO_2.

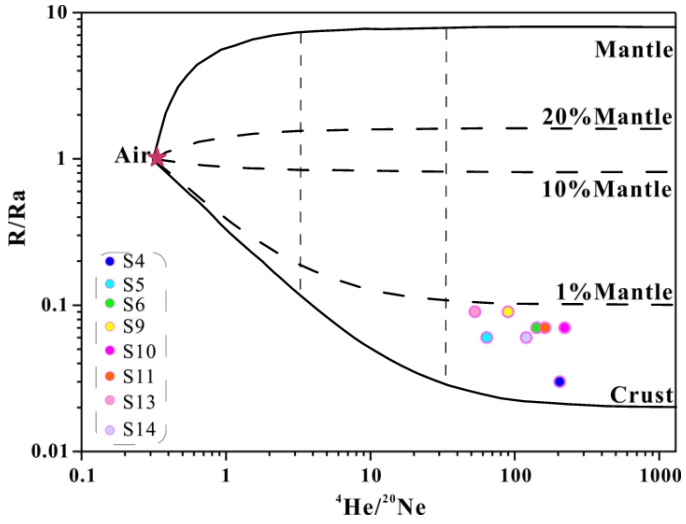

Figure 11. Plot of ^{3}He/^{4}He vs. ^{4}He/ ^{20}Ne average ratios. Mixing lines between the atmosphere and upper mantle, as well as between the atmosphere and crust, were calculated using the following end-member compositions. air: ^{3}He/^{4}He = 1.4 × 10^{-6}; ^{4}He/^{20}Ne = 0.318, upper mantle: ^{3}He/^{4}He = 12 × 10^{-6}; ^{4}He/^{20}Ne = 100,000, old continental crust: ^{3}He/^{4}He = 0.02 × 10^{-6}; ^{4}He/^{20}Ne = 100,000 [69].

The chemical inertness and incompatible nature of helium make it particularly valuable for tracing fluid origins, providing complementary information to carbon isotope data The $CO_2/^3$He versus δ^{13}C-CO_2 cross-plot (Figure 11) clearly clusters the samples within the crustal domain, providing robust confirmation of the shallow water–rock interaction processes inferred from other geochemical indicators. This integrated interpretation demonstrates that the thermal fluids are predominantly crustal in origin, with minimal mantle influence, consistent with the regional tectonic framework and geological setting.

5.3.2. Sources of CO_2 Gases

As the primary component of the deep fluids, CO_2 typically acts as the carrier gas for noble gases like helium [70]. To delineate its provenance, we employed a plot of $CO_2/^3$He versus δ^{13}C-CO_2 (Figure 12) [42,66,67,71]. All samples plot within the crustal domain and point unequivocally to a source dominated by the dissolution of carbonate rocks (limestone), with minimal contributions from mantle or organic sedimentary sources.

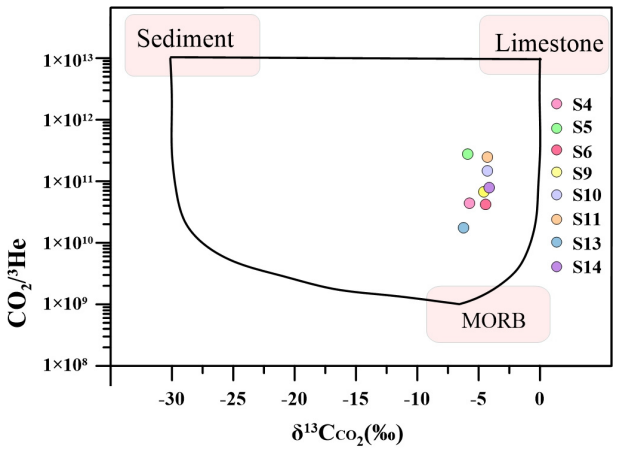

Figure 12. Plot of $CO_2/^3$He vs. $\delta^{13}Cco_2$ for the bubble gas samples. Plot of $CO_2/^3$He vs. $\delta^{13}Cco_2$, $(CO_2/^3He)_{sed.}$ = 10^{13}, $(^{13}Cco_2)_{sed.}$ =−30‰, $(CO_2/^3He)_{Lim.}$ = 10^{13}, $(^{13}Cco_2)_{Lim.}$ = 0 ‰, $(CO_2/^3He)_{MORB}$ = 1.5 × 10^9, ($^{13}Cco_2$) Mantle = −6.5 ‰ [70].

This interpretation is in full agreement with the hydrochemical characteristics of the associated thermal waters established in Section 5.1. The dominant HCO_3-Ca-Mg hydrochemical type, the lack of enrichment in characteristic hydrothermal trace elements (e.g., Li, B), and the supersaturation with respect to carbonate minerals such as calcite and dolomite (SI > 1) collectively form a cohesive body of evidence [72]. This demonstrates that the fluid system is controlled by carbonate dissolution processes within the shallow crust, rather than by inputs from deep magmatic or mantle fluids.

Therefore, the geochemical evidence from both the gas and water phases converges to a single, self-consistent conclusion: the volatiles in the MJF are predominantly crustal in origin, and the key driving mechanism is the dissolution of carbonate rocks by CO_2-rich fluids.

5.4. Hydrogeochemical Response to Tectonic Activity: From Spatial Distribution to Temporal Evolution

Tectonic activities such as earthquakes can significantly alter subsurface fluid circulation systems, and their effects should be manifested in both the spatial distribution and temporal evolution of fluid geochemical characteristics. Spatially, the distribution of the 22 hot springs sampled in this study along the MJF is non-random, exhibiting a macroscopic correlation with regional seismic activity (including magnitude and focal depth) (Figure 13). The figure aims to demonstrate a spatial correlation, not a direct causal link, between the fluid system and seismicity. This presents an important insight: despite the occurrence of deep-focus, high-magnitude seismicity, the geochemical signature of the hot springs (e.g., HCO_3-Ca-Mg type, crustal helium isotope ratios) indicates a fluid origin dominated by shallow crustal processes, primarily carbonate dissolution driven by water–rock interaction. The earthquakes do not appear to trigger significant upward migration of deep, mantle-derived fluids. Instead, the spatial correlation suggests that the seismic activity and the geothermal system are both manifestations of the same active tectonic setting. The seismogenic processes likely enhance fracture permeability, which in turn influences the intensity of water–rock interaction in the shallow crust and the mixing ratio with shallow groundwater, ultimately modulating the hydrogeochemical composition observed at the surface. This suggests that the fluid system of the entire fault zone is tightly coupled with seismic activity.

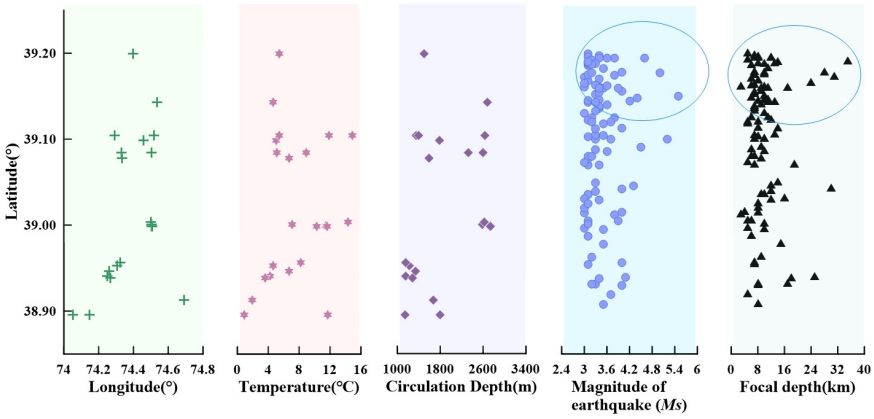

Figure 13. Spatial distribution of temperature, circulation depth of 22 hot springs, earthquake magnitude and focal depth.

5.5. Correlation Between Hydrogeochemical Changes and Earthquakes

Earthquakes and tectonic activities significantly modify hot spring circulation depth, thermal reservoir temperature, and deep fluid dynamics by disrupting the inherent water–rock equilibrium, thereby intensifying water–rock interactions [7]. Such physicochemical alterations are directly reflected in the ionic composition and hydrogen–oxygen isotopic

signatures of spring water [7,73,74]. Multiple studies have documented significant hydrogeochemical shifts in hot spring fluids before and after seismic events. These variations are attributed to altered water–rock reaction intensities and mixing of subsurface fluids from distinct sources [75–78].

Our preceding analysis has established two key points. First, we have systematically characterized the "static baseline" of the geothermal fluid system within the Muji Fault Zone (MJF). This system is characterized by HCO_3-Ca·Mg type water, which is recharged by meteoric water, dominated by the dissolution of carbonate rocks, and exhibits a chemically "immature" state due to mixing with shallow cold water. Second, we have revealed a significant "spatial coupling" between the distribution of this geothermal system and regional seismic activity, suggesting a strong intrinsic link between the fluid system and tectonic activity.

However, these static characteristics and spatial correlations alone are insufficient to fully substantiate the dynamic interaction between them. To verify this coupling, the critical step is to capture the temporal evolution of the geothermal system during processes of seismic stress adjustment. Therefore, our research focus shifts from broad regional characteristics to two representative springs that have been under long-term, continuous monitoring: Bulake (BLK) and Taheman (THM). These two springs were selected because: (1) they are typical of the study area, with hydrochemical compositions that are entirely consistent with the regional characteristics analyzed previously; and (2) they benefit from valuable, high-frequency (thrice-daily) continuous monitoring data, which provides the opportunity to capture subtle dynamic fluid changes before and after earthquakes.

Drawing on experience from other tectonically active regions, such as the North Tianshan Orogenic Belt [79], we selected hydrogen and oxygen isotopes (δD, $\delta^{18}O$) and major ions (Na^+, Cl^-, SO_4^{2-})—parameters known to be highly sensitive to changes in tectonic stress—as key response indicators. The monitoring results for these parameters are presented in Figure 14 and Table 4.

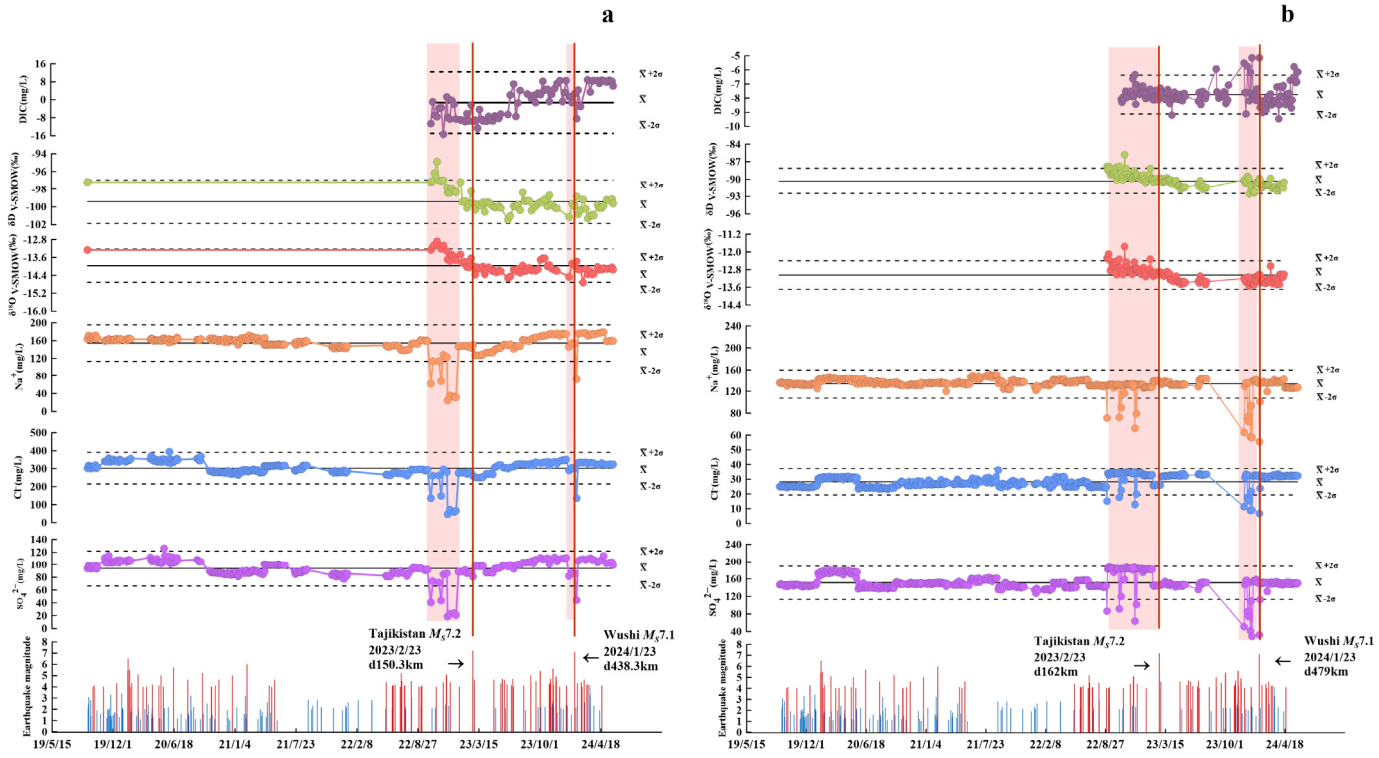

Figure 14. Time changes in major ions and hydrogen and oxygen isotopes of BLK (**a**) and THM (**b**).

Table 4. The anomalies of 2 hot springs before the 2023 *Ms*7.2 earthquake in Tajikistan and 2024 *Ms*7.1 earthquake in Wushi.

Earthquake	Hot Spring	Anomaly Amplitude (Days Before the Earthquake)					
		SO_4^{2-}	Cl^-	Na^+	$\delta^{18}O$	δD	$\delta^{13}C$ (DIC)
Tajikistan *Ms*7.2 2023/2/23	BLK d150.3 km	−5.10σ (120D)	−3.78σ (120D)	−6.65σ (120D)	3.61σ (99D)	2.84σ (99D)	−2.05σ (76D)
	THM d162 km	−3.41σ (155D)	−3.27σ (155D)	−4.77σ (155D)	4.11σ (94D)	3.91σ (94D)	1.99σ (63D)
Wushi *Ms*7.1 2024/1/23	BLK d480.3 km	−1.12σ (18D)	−0.28σ (18D)	−0.64σ (18D)	−1.41σ (12D)	−1.32σ (12D)	1.42σ (28D)
	THM d479 km	−5.26σ (49D)	−4.323σ (49D)	−6.73σ (49D)	−2.05σ (32D)	−1.52σ (32D)	3.77σ (94D)

5.5.1. Consistency with Existing Hydrogeochemical Precursor Mechanisms

Dynamic monitoring of the two representative springs (BLK and THM) clearly reveals the sensitive response of the geothermal system to seismic activity. Before the *Ms*7.2 Tajikistan earthquake in 2023 and the *Ms*7.1 Wushi earthquake in 2024, the most central and consistent observation was the synchronous and significant decrease in the concentrations of major ions such as Na^+, Cl^-, and SO_4^{2-}. While our original sampling campaign lacked continuous monitoring of seasonal parameters (e.g., precipitation, spring discharge, temperature), we mitigated this limitation by integrating long-term monitoring data from two key springs (BLK and THM) covering May 2019–April 2024.

Analysis of this extended dataset showed that during periods of low or no seismic activity, ion concentrations (e.g., Na^+, Cl^-, SO_4^{2-}) displayed minimal fluctuations around baseline values, with deviations consistently within one standard deviation of the mean. This stability indicates that while seasonal factors may induce background variability, their impact on seismically related anomalies is negligible. Notably, the prominent pre-seismic negative excursions detected prior to the 2023 Tajikistan and 2024 Wushi earthquakes far exceeded the amplitude of seasonal variations, highlighting the dominance of tectonic stress over hydrometeorological effects.

This points to a unified hydrogeochemical response mechanism: the mixing and dilution by shallow cold water driven by tectonic stress. Specifically, during the pre-seismic regional stress accumulation phase, the permeability of the fault zone and its secondary fractures increases, providing enhanced pathways for the downward percolation of less mineralized shallow cold water (sourced from meteoric precipitation or snowmelt) [35]. The accelerated influx of a large volume of this cold water leads to more efficient mixing with the relatively ion-rich geothermal fluids circulating at depth. This results in a net dilution effect on the reservoir fluid, which is directly manifested as a decrease in the major ion concentrations of the surface springs [78].

Changes in hydrogen and oxygen isotopes provide corroborating evidence for this mixing process. The synchronous decrease in δD and $\delta^{18}O$ values observed at the BLK monitoring point before the Wushi earthquake is consistent with the trend of ion concentration changes, jointly confirming an increased contribution from isotopically more "negative" shallow meteoric water to the system. Concurrently, variations in dissolved inorganic carbon isotopes ($\delta^{13}C_{DIC}$) reveal more subtle, superimposed local geochemical processes [80–84].The different response patterns of $\delta^{13}C_{DIC}$ at THM and BLK indicate that although a unified physical dilution process is the dominant mechanism explaining the anomalies in major ions and water isotopes, the final response of specific geochemical indicators is also modulated by local lithological differences and varying carbon sources.

5.5.2. Distance-Dependent Anomaly Intensity and Temporal Patterns

Within the framework of this unified dilution mechanism, the spatiotemporal differences in the anomalous responses reveal tectonic implications that go deeper than precursor

identification itself. A conventional concept is the "distance effect," wherein the intensity of a seismic response attenuates with increasing epicentral distance. The response pattern at the Bulake (BLK) monitoring point largely conforms to this conventional expectation: it exhibited a strong anomaly in response to the Tajikistan earthquake, approximately 150 km away, whereas its response to the Wushi earthquake, at a distance of about 480 km, was markedly weaker. This indicates that for the tectonic setting of the BLK site, the principle of stress response intensity decreasing significantly with distance is applicable.

However, the response pattern at the Taheman (THM) monitoring point deviates significantly from this conventional understanding, thereby highlighting the critical control of tectonic structure. The THM site not only responded strongly to the nearer Tajikistan earthquake but also displayed an extremely pronounced anomaly in response to the much more distant Wushi earthquake. Furthermore, before the Tajikistan earthquake, the anomaly at THM (appearing 155 days prior) emerged earlier than at BLK (120 days prior). These two phenomena—the anomalous "cross-distance" high intensity and the response "precedence"—collectively point to one conclusion: THM is situated in a tectonically highly sensitive and special location, such as a fault intersection. Such structural nodes are preferential zones for regional stress concentration and efficient stress transfer.

Therefore, the differentiated responses of these two monitoring points to two different earthquakes reveal the complexity of regional stress transfer. A comparative analysis indicates that stress transfer within the Earth's crust is highly anisotropic, with its efficiency and pathways primarily controlled by the geometric distribution and connectivity of major fault systems. The strong response of the THM site to a far-field earthquake corroborates the high sensitivity of its tectonic location, which is capable of transmitting far-field stress changes from specific directions with low attenuation. Ultimately, these anomalous spatiotemporal distribution patterns constitute robust geochemical evidence for revealing the mechanical properties of the regional fault network and assessing the stress coupling relationships between different fault systems.

5.6. Fluid Circulation Model of Hot Spring in the MJF

Investigating the origin and circulation of hot springs within active fault zones and understanding their hydrogeochemical characteristics are essential for analyzing the mechanisms underlying variations in chemical parameters, which is crucial for precursor research [85,86]. Integrating the preceding analyses of hydrochemistry, gas origins, and tectonic response, we establish a comprehensive conceptual model for the geothermal fluid system of the MJF (Figure 15). This model not only explains the system's stable characteristics during the "inter-seismic" period but, more critically, elucidates its dynamic response mechanism during the "pre-seismic" phase.

1. Inter-seismic Fluid Circulation Model

The model originates with recharge from high-altitude meteoric precipitation. This water infiltrates downward along the MJF and its secondary fracture network, entering deep circulation. During circulation, the fluid is heated by the geothermal gradient, reaching reservoir temperatures of 67 to 155 °C. Concurrently, it undergoes intense water–rock interaction, the core of which is the dissolution of carbonate rocks. This process not only forms the HCO_3-Ca-Mg type water observed at the surface but also enriches the fluid with gases such as CO_2 and He, which bear a distinct crustal signature derived from carbonate dissolution. Subsequently, these heated, mineralized, and gas-charged deep fluids ascend along fault conduits under the regional compressional stress field. Upon approaching the surface, they mix with shallow, cold, low-TDS (Total Dissolved Solids) groundwater, ultimately causing the discharged spring waters to exhibit a chemically "immature" state.

2. Fluid Dynamic Response Model Under Intense Tectonic Stress Perturbation

When regional tectonic stress accumulates (driven by the ongoing India–Eurasia plate convergence), the relatively stable circulatory system described above is perturbed. The changing stress field enhances the permeability of the MJF or creates new micro-fractures, effectively opening more conduits for shallow cold water to invade downward. Consequently, a greater volume of low-ion-concentration shallow water mixes more efficiently with the deep hot water system than during periods of weak tectonic activity, producing a strong dilution effect on the original reservoir fluid. This dilution directly leads to the significant negative anomalies in key ions (Na^+, Cl^-, and SO_4^{2-}) observed at the BLK and THM monitoring sites—anomalies that reflect the dynamic adjustment of the geothermal fluid system in response to tectonic stress changes [68,86,87].

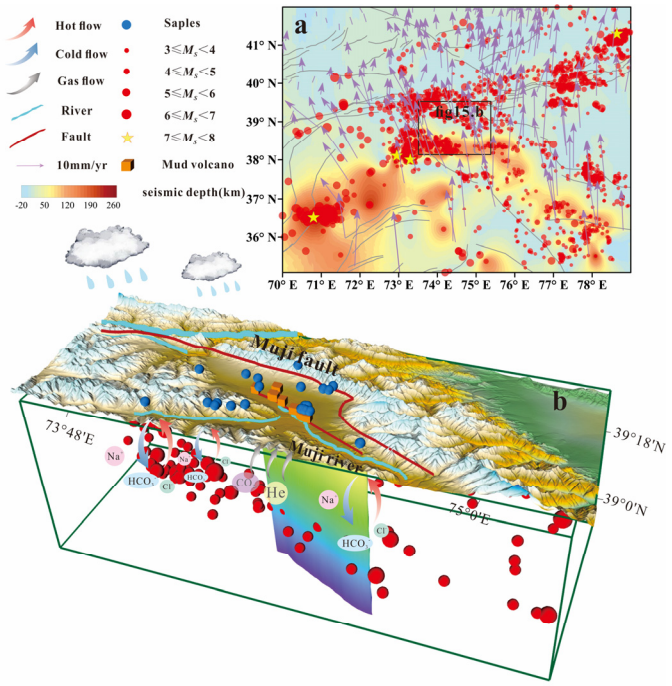

Figure 15. The source of mantle and the conceptual model of crustal flow in MJF. (**a**) Geographic location and stress field of the study area; (**b**) Conceptual model of fluid circulation in the study area. GPS velocity field from Zheng et al. [88].

In summary, this integrated "fault-spring" fluid response model successfully connects deep tectonic stress changes (the driving factor) with observable surface hydrogeochemical anomalies (the response) through a clear physico-chemical process (stress-enhanced permeability → cold water infiltration and mixing → fluid dilution) [3,39,75,86]. It provides a geochemical perspective for understanding the coupling relationship between tectonic activity and geothermal fluid dynamics in the MJF, and confirms that long-term monitoring of key springs along this fault is an effective means of capturing the dynamic changes in fault-controlled geothermal systems.

6. Conclusions

Based on comprehensive geochemical analysis of 22 hot springs along the MJF, we have established a conceptual model of subsurface fluid circulation with the following key findings:

(1) Hydrochemical and isotopic characteristics collectively indicate that the geothermal waters in the study area are primarily recharged by meteoric precipitation. During deep circulation, the waters form a HCO_3-Ca-Mg type through water–rock interaction dominated by the dissolution of carbonate rocks. These deep hot waters, ascending

along the fault zone under compressional stress, ultimately mix with shallow cold water, leading to their chemically "immature" signature.

(2) Na^+, Cl^-, and SO_4^{2-} are sensitive indicators exhibiting significant pre-seismic anomalies in the study area. The characteristic decrease in these ion concentrations observed before strong earthquakes can be attributed to a coupled "enhanced-permeability–cold-water-mixing–dilution" mechanism: pre-seismic stress accumulation enhances fault zone permeability, allowing shallow, low-TDS cold water to mix with and dilute the deep geothermal fluid more efficiently.

(3) A conceptual model of fluid circulation and seismic response was established, explaining the entire fluid pathway from recharge to discharge and revealing its dynamic response to changes in tectonic stress. The observed hydrochemical changes effectively track fluid–tectonic interactions. Future research should focus on expanding long-term monitoring networks to include more springs and mud volcanoes, quantifying the sensitivity of geochemical indicators to different magnitudes of tectonic disturbance, and integrating geophysical data (e.g., GPS, InSAR) to further refine the fluid–tectonic–seismic interaction mechanism in fault-controlled geothermal systems.

Supplementary Materials: The following supporting information can be downloaded at https://www.mdpi.com/article/10.3390/w17223241/s1, Table S1: Field and analytical data of major elements and stable isotopes (δD, $\delta^{18}O$) on water samples.

Author Contributions: S.C.: Writing—review and editing, Writing—original draft, Methodology, Formal analysis, Conceptualization. F.Z.: Project administration, Investigation, Funding acquisition. X.Z.: Writing—review and editing, Project administration, Investigation, Funding acquisition. J.L.: Writing—review and editing, Investigation. J.T.: Writing—review and editing, Methodology. Z.Z.: Writing—review and editing, Methodology. Y.W.: Writing—review and editing, Data curation. B.Y.: Writing—review and editing, Formal analysis, Data curation. G.X.: Formal analysis, Data curation. J.D.: Formal analysis, Data curation. M.H.: Formal analysis, Data curation. H.Y.: Formal analysis, Data curation. R.L.: Formal analysis, Data curation. W.Z.: Formal analysis, Data curation. K.S.: Formal analysis, Data curation. C.W.: Formal analysis, Data curation. W.Y.: Formal analysis, Data curation. R.M.: Formal analysis, Data curation. All authors have read and agreed to the published version of the manuscript.

Funding: This research was funded by the Open Fund of Observation and Research Station of Tianjin Low-Medium Temperature Geothermal Resources, Ministry of Natural Resources (No. TJDRYWZ-202401), the Deep-land National Science and Technology Major Project (Grants 2024ZD1000503, 2024ZD1003503), Deep Earth Probe and Mineral Resources Exploration—National Science and Technology Major Project (2024ZD1000500), National Key Research and Development Project (2023YFC3012005-1), the National Natural Science Foundation of China (41673106).

Data Availability Statement: The raw data supporting the conclusions of this article will be made available by the authors, without undue reservation.

Conflicts of Interest: The authors declare no conflicts of interest.

Abbreviations

The following abbreviations are used in this manuscript:

MJF	Muji Fault Zone
THM	Tahman Spring
BLK	Bulake Village Spring
SFKM	Southern Fault of the Kungai Mountains
δD	Deuterium isotope ratio (relative to V-SMOW)
$\delta^{18}O$	Oxygen-18 isotope ratio (relative to V-SMOW)

$\delta^{13}C$ DIC	$\delta^{13}C$ in dissolved inorganic carbon
$\delta^{13}C$ CO_2	$\delta^{13}C$ in CO_2
RSD	Relative Standard Deviation
TDS	Total dissolved solids
GMWL	Global Meteoric Water Line
LMWL	Local Meteoric Water Line
EF_i	Enrichment Factors
SI	Saturation Index

References

1. Nishio, Y. Geofluid research using lithium isotopic tool advances understanding of whole crustal activity. *J. Jpn. Assoc. Hydrol. Sci.* **2013**, *43*, 119–135. [CrossRef]
2. Zhao, D.; Kanamori, H.; Negishi, H.; Wiens, D. Tomography of the source area of the 1995 Kobe earthquake: Evidence for fluids at the hypocenter? *Science* **1996**, *274*, 1891–1894. [CrossRef] [PubMed]
3. Zandvakili, Z.; Nishio, Y.; Sano, Y. Geofluid behavior prior to the 2018 Hokkaido Eastern Iburi earthquake: Insights from groundwater geochemistry. *Prog. Earth Planet. Sci.* **2024**, *11*, 32. [CrossRef]
4. Claesson, L.; Skelton, A.; Graham, C.; Dietl, C.; Mörth, M.; Torssander, P.; Kockum, I. Hydrogeochemical changes before and after a major earthquake. *Geology* **2004**, *32*, 641–644. [CrossRef]
5. Paudel, S.R.; Banjara, S.P.; Wagle, A.; Freund, F.T. Earthquake chemical precursors in groundwater: A review. *J. Seismol.* **2018**, *22*, 1293–1314. [CrossRef]
6. Hosono, T.; Saltalippi, C.; Jean, J.-S. Coseismic hydro-environmental changes: Insights from recent earthquakes. *J. Hydrol.* **2020**, *585*, 124799. [CrossRef]
7. Skelton, A.; Liljedahl-Claesson, L.; Wasteby, N.; Andren, M.; Stockmann, G.; Sturkell, E.; Morth, C.M.; Stefansson, A.; Tollefsen, E.; Siegmund, H.; et al. Hydrochemical Changes Before and After Earthquakes Based on Long-Term Measurements of Multiple Parameters at Two Sites in Northern Iceland—A Review. *J. Geophys. Res.-Solid Earth* **2019**, *124*, 2702–2720. [CrossRef]
8. Na, J.; Jiang, X.; Shi, Z.; Chen, Y. Reactive Transport Process of Earthquake-induced Hydro-chemical Changes in Guanding Thermal Spring, Western Sichuan, China. *Acta Geol. Sin.-Engl. Ed.* **2024**, *98*, 241–249. [CrossRef]
9. Li, B.; Shi, Z.; Wang, G.; Liu, C. Earthquake-related hydrochemical changes in thermal springs in the Xianshuihe Fault zone, Western China. *J. Hydrol.* **2019**, *579*, 124175. [CrossRef]
10. Evans, J.P.; Forster, C.B.; Goddard, J.V. Permeability of fault-related rocks, and implications for hydraulic structure of fault zones. *J. Struct. Geol.* **1997**, *19*, 1393–1404. [CrossRef]
11. Sibson, R.H. Fluid involvement in normal faulting. *J. Geodyn.* **2000**, *29*, 469–499. [CrossRef]
12. Zucchi, M. Faults controlling geothermal fluid flow in low permeability rock volumes: An example from the exhumed geothermal system of eastern Elba Island (northern Tyrrhenian Sea, Italy). *Geothermics* **2020**, *85*, 101765. [CrossRef]
13. Cox, S.C.; Menzies, C.D.; Sutherland, R.; Denys, P.H.; Chamberlain, C.; Teagle, D.A. Changes in hot spring temperature and hydrogeology of the Alpine Fault hanging wall, New Zealand, induced by distal South Island earthquakes. In *Crustal Permeability*; Wiley: Hoboken, NJ, USA, 2012; pp. 228–248.
14. Leloup, P.H.; Lacassin, R.; Tapponnier, P.; Scharer, U.; Zhong, D.L.; Liu, X.H.; Zhang, L.S.; Ji, S.C.; Trinh, P.T. The Ailao Shan-Red River shear zone (Yunnan, China), Tertiary transform boundary of Indochina. *Tectonophysics* **1995**, *251*, 3–84. [CrossRef]
15. Zhang, J.; Kong, Y. Rheological characteristics of lithospheric mantle in the Pamir Plateau and temperature structure of its northeastern margin: Results of the Third Xinjiang Comprehensive Scientific Expedition on Geothermal Science. *Chin. J. Geophys.-Chin. Ed.* **2025**, *68*, 199–212. [CrossRef]
16. Chelnokov, G.; Lavrushin, V.; Bragin, I.; Abdullaev, A.; Aidarkozhina, A.; Kharitonova, N. Geochemistry of Thermal and Cold Mineral Water and Gases of the Tien Shan and the Pamir. *Water* **2022**, *14*, 838. [CrossRef]
17. Chen, F.; Lin, J.; He, G.; Wang, S.; Huang, X.; Zhao, B.; Wang, S.; Han, Y.; Qi, S. Analysis of geothermal resources in the northeast margin of the Pamir plateau. *Geothermics* **2025**, *127*, 103254. [CrossRef]
18. Li, Y.; Pang, Z.; Yang, F.; Yuan, L.; Tang, P. Hydrogeochemical characteristics and genesis of the high-temperature geothermal system in the Tashkorgan basin of the Pamir syntax, western China. *J. Asian Earth Sci.* **2017**, *149*, 134–144. [CrossRef]
19. Zhuang, S.; Zhou, X.; Li, P.; Shi, Z.; Zhu, C.; Yan, Y. Environmental Hydrogeochemical Characteristics of Hot Springs in Tashkurgan Fault Zone of Xinjiang, China. *J. Earch Sci. Environ.* **2022**, *44*, 699–712.
20. Liu, J.; Wu, C.; Zhang, B. The attributes and characteristics of "Muji volcano group" in Xinjiang. *Acta Geol. Sin.* **2024**, *98*, 1637–1648.
21. Chen, R.; Li, J.; Liu, D. InSAR study of current tectonie deformation and seismie hazard analysis ofthe Kongur tension system in northeastern Pamir's. *Bull. Surv. Mapp* **2024**, 79. [CrossRef]

22. Zhao, B.; Wang, S.; Chen, F.; He, G.; Huang, X.; Wang, S.; Qi, S. Hydrogeochemical Characteristics and Genesis of Medium-High Temperature Geothermal System in Northeast Margin of Pamir Plateau. *Editor. Comm. Earth Sci.-J. China Univ. Geosci.* **2024**, *49*, 3736–3748.
23. Chen, F.; Qi, S.; Wang, S.; He, G.; Zhao, B. Unraveling the Genesis of the Geothermal System at the Northeastern Edge of the Pamir Plateau. *Water* **2023**, *15*, 3583. [CrossRef]
24. Yin, A.; Harrison, T.M. Geologic evolution of the Himalayan-Tibetan orogen. *Annu. Rev. Earth Planet. Sci.* **2000**, *28*, 211–280. [CrossRef]
25. Kumar, V.; Rai, S.S.; Hawkins, R.; Bodin, T. Seismic imaging of crust beneath the western Tibet-Pamir and Western Himalaya using ambient noise and earthquake data. *J. Geophys. Res. Solid Earth* **2022**, *127*, e2021JB022574. [CrossRef]
26. Zhang, J.; Song, X.; Wu, D.; Shan, X. Present-Day Tectonic Deformation Characteristics of the Northeastern Pamir Margin Constrained by InSAR and GPS Observations. *Remote Sens.* **2024**, *16*, 4771. [CrossRef]
27. Li, T.; Schoenbohm, L.M.; Chen, J.; Yuan, Z.; Feng, W.; Li, W.; Xu, J.; Owen, L.A.; Sobel, E.R.; Zhang, B.; et al. Cumulative and Coseismic (During the 2016 M_w 6.6 Aketao Earthquake) Deformation of the Dextral-Slip Muji Fault, Northeastern Pamir Orogen. *Tectonics* **2019**, *38*, 3975–3989. [CrossRef]
28. Bie, L.; Hicks, S.; Garth, T.; Gonzalez, P.; Rietbrock, A. 'Two go together': Near-simultaneous moment release of two asperities during the 2016 Mw 6.6 Muji, China earthquake. *Earth Planet. Sci. Lett.* **2018**, *491*, 34–42. [CrossRef]
29. Ma, Y.; Qiao, X.; Chen, W.; Zhou, Y. Source model of 2016 Mw 6.6 Aketao earthquake, Xinjiang derived from Sentinel-1 InSAR observation. *Geod. Geodyn.* **2018**, *9*, 372–377. [CrossRef]
30. Zhang, X.; Xu, L.-S.; Li, L.; Yi, L.; Feng, W. Confirmation of the double-asperity model for the 2016 MW 6.6 Akto earthquake (NW China) by seismic and InSAR data. *J. Asian Earth Sci.* **2019**, *184*, 103998. [CrossRef]
31. Bloch, W.; Schurr, B.; Yuan, X.; Ratschbacher, L.; Reuter, S.; Kufner, S.K.; Xu, Q.; Zhao, J. Structure and stress field of the lithosphere between Pamir and Tarim. *Geophys. Res. Lett.* **2021**, *48*, e2021GL095413. [CrossRef]
32. Chen, J.; Li, T.; Sun, J.; Fang, L.; Yao, Y.; Li, Y.; Wang, H.; Fu, B. Coseismic surface ruptures and seismogenic Muji fault of the 25 November 2016 Arketao MW 6.6 earthquake in northern Pamir. *Seismol. Geol.* **2016**, *38*, 1160–1174.
33. Steinshouer, D.W.; Qiang, J.; McCabe, P.J.; Ryder, R.T. *Maps Showing Geology, Oil and Gas Fields, and Geologic Provinces of the Asia Pacific Region*; 2331-1258; US Geological Survey: Fairfax County, VA, USA, 1999.
34. Zhonghe, P. Mechanism of water cycle changes and implications on water resources regulation in Xinjiang Uygur autonomous region. *Quat. Sci.* **2014**, *34*, 907–917.
35. Zeng, Z.; Zhou, X.; Dong, J.; Li, J.; He, M.; Tian, J.; Wang, Y.; Yan, Y.; Yao, B.; Cui, S.; et al. Seismic Signals of the Wushi MS7.1 Earthquake of 23 January 2024, Viewed Through the Angle of Hydrogeochemical Characteristics. *Appl. Sci.* **2025**, *15*, 4791. [CrossRef]
36. *ISO 11885: 2007*; Water Quality-Determination of Selected Elements by Inductively Coupled Plasma Optical Emission Spectrometry (ICP-OES). Beuth Verlag GmbH: Berlin, Germany, 2009.
37. Assayag, N.; Rivé, K.; Ader, M.; Jézéquel, D.; Agrinier, P. Improved method for isotopic and quantitative analysis of dissolved inorganic carbon in natural water samples. *Rapid Commun. Mass Spectrom.* **2006**, *20*, 2243–2251. [CrossRef]
38. Alixiati, Y.; Liu, D.; Li, J.; Li, R.; Abudutayier, Y.; Liu, X.; Zhu, Z.; Li, G.; Chen, L. Analysis of Gravity Changes Before and After Aktao Earthquake with Ms 6.7, 2016. *Inland Earthq.* **2017**, *31*, 198–206. [CrossRef]
39. Yan, Y.; Zhang, Z.; Zhou, X.; Wang, G.; He, M.; Tian, J.; Dong, J.; Li, J.; Bai, Y.; Zeng, Z.; et al. Geochemical characteristics of hot springs in active fault zones within the northern Sichuan-Yunnan block: Geochemical evidence for tectonic activity. *J. Hydrol.* **2024**, *635*, 131179. [CrossRef]
40. Butler, J.N. *Ionic Equilibrium: Solubility and pH Calculations*; John Wiley & Sons: Hoboken, NJ, USA, 1998.
41. Chun-hui, C.; Ming-jie, Z.; Qing-yan, T.; Zong-gang, L.; Yang, W.; Li, D.; Zhong-ping, L. Geochemical characteristics and implications of shale gas in Longmaxi Formation, Sichuan Basin, China. *Nat. Gas Geosci.* **2015**, *26*, 1604–1612.
42. Wang, S.; Zhou, X.; Tian, J.; He, M.; Li, J.; Dong, J.; Li, L.; Li, Z.; Xing, L.; Zheng, G. Constraints on geological structures and dynamics along the Tian Shan-Pamir orogenic belt with helium isotopes in hot springs. *Appl. Geochem.* **2024**, *160*, 105859. [CrossRef]
43. Sano, Y.; Wakita, H. Geographical distribution of 3He/4He ratios in Japan: Implications for arc tectonics and incipient magmatism. *J. Geophys. Res. Solid Earth* **1985**, *90*, 8729–8741. [CrossRef]
44. Appelo, C.A.J.; Postma, D. *Geochemistry, Groundwater and Pollution*, 2nd ed.; Balkema: Rotterdam, The Netherlands, 2005.
45. Hanshaw, B.B.; Back, W. Major geochemical processes in the evolution of carbonate—Aquifer systems. *J. Hydrol.* **1979**, *43*, 287–312. [CrossRef]
46. Morse, J.W.; Arvidson, R.S.; Lüttge, A. Calcium carbonate formation and dissolution. *Chem. Rev.* **2007**, *107*, 342–381. [CrossRef]
47. Giggenbach, W.F. Geothermal solute equilibria. derivation of Na-K-Mg-Ca geoindicators. *Geochim. Cosmochim. Acta* **1988**, *52*, 2749–2765. [CrossRef]

48. Arnórsson, S.; Stefánsson, A.; Bjarnason, J.O. Fluid-fluid interactions in geothermal systems. *Rev. Mineral. Geochem.* **2007**, *65*, 259–312. [CrossRef]
49. Craig, H. Isotopic variations in meteoric waters. *Science* **1961**, *133*, 1702–1703. [CrossRef] [PubMed]
50. Blasch, K.W.; Bryson, J.R. Distinguishing sources of ground water recharge by using δ^2H and $\delta^{18}O$. *Groundwater* **2007**, *45*, 294–308. [CrossRef]
51. Kortelainen, N.M.; Karhu, J.A. Regional and seasonal trends in the oxygen and hydrogen isotope ratios of Finnish groundwaters: A key for mean annual precipitation. *J. Hydrol.* **2004**, *285*, 143–157. [CrossRef]
52. Wang, S.; Zhang, M.; Hughes, C.E.; Zhu, X.; Dong, L.; Ren, Z.; Chen, F. Factors controlling stable isotope composition of precipitation in arid conditions: An observation network in the Tianshan Mountains, central Asia. *Tellus B Chem. Phys. Meteorol.* **2016**, *68*, 26206. [CrossRef]
53. Tian, L.; Yao, T.; MacClune, K.; White, J.; Schilla, A.; Vaughn, B.; Vachon, R.; Ichiyanagi, K. Stable isotopic variations in west China: A consideration of moisture sources. *J. Geophys. Res. Atmos.* **2007**, *112*. [CrossRef]
54. Tian, L.; Yao, T.; Numaguti, A.; Sun, W. Stable isotope variations in monsoon precipitation on the Tibetan Plateau. *J. Meteorol. Soc. Jpn. Ser. II* **2001**, *79*, 959–966. [CrossRef]
55. Pang, Z.; Kong, Y.; Li, J.; Tian, J. An isotopic geoindicator in the hydrological cycle. *Procedia Earth Planet. Sci.* **2017**, *17*, 534–537. [CrossRef]
56. Pang, Z.; Kong, Y.; Froehlich, K.; Huang, T.; Yuan, L.; Li, Z.; Wang, F. Processes affecting isotopes in precipitation of an arid region. *Tellus B Chem. Phys. Meteorol.* **2011**, *63*, 352–359. [CrossRef]
57. Gong, D.-X.; Wu, C.-H.; Zou, H.; Zhou, X.; Zhou, Y.; Tan, H.-Q.; Yue, X.-Y. Provenance analysis of Late Triassic turbidites in the eastern Songpan–Ganzi Flysch Complex: Sedimentary record of tectonic evolution of the eastern Paleo-Tethys Ocean. *Mar. Pet. Geol.* **2021**, *126*, 104927. [CrossRef]
58. Yang, H.; Wu, X.; Cui, H.; Wang, W.; Cheng, Y.; Gong, X.; Luo, X.; Lin, Q. Formation Mechanism of Muji Travertine in the Pamirs Plateau, China. *Minerals* **2024**, *14*, 1192. [CrossRef]
59. Bufe, A.; Hovius, N.; Emberson, R.; Rugenstein, J.K.; Galy, A.; Hassenruck-Gudipati, H.J.; Chang, J.-M. Co-variation of silicate, carbonate and sulfide weathering drives CO_2 release with erosion. *Nat. Geosci.* **2021**, *14*, 211–216. [CrossRef]
60. Cui, R.; Cui, Q.; Zhou, Y. smic velocity structures and deep dynamic processes in the crust and mantle beneath the Tianshan Orogenic Belt. *Rev. Geophys. Planet. Phys.* **2024**, *55*, 381–398. [CrossRef]
61. Peng, X.; Hongbing, T.; Yanfei, Z.; Wenjie, Z. Geochemical characteristics and source mechanism of geothermal water in Tethys Himalaya belt. *Geol. China* **2018**, *45*, 1142–1154.
62. Parkhurst, D.L.; Appelo, C. *User's Guide to PHREEQC (Version 2): A Computer Program for Speciation, Batch-Reaction, One-Dimensional Transport, and Inverse Geochemical Calculations*; US Geological Survey: Fairfax County, VA, USA, 1999.
63. Arnórsson, S.; Gunnlaugsson, E.; Svavarsson, H. The chemistry of geothermal waters in Iceland. III. Chemical geothermometry in geothermal investigations. *Geochim. Cosmochim. Acta* **1983**, *47*, 567–577. [CrossRef]
64. Fournier, R. Chemical geothermometers and mixing models for geothermal systems. *Geothermics* **1977**, *5*, 41–50. [CrossRef]
65. Jiang, G.-Z.; Gao, P.; Rao, S.; Zhang, L.-Y.; Tang, X.-Y.; Huang, F.; Zhao, P.; Pang, Z.-H.; He, L.-J.; Hu, S.-B. Compilation of heat flow data in the continental area of China. *Chin. J. Geophys.* **2016**, *59*, 2892–2910.
66. Kurz, M.D.; Meyer, P.S.; Sigurdsson, H. Helium isotopic systematics within the neovolcanic zones of Iceland. *Earth Planet. Sci. Lett.* **1985**, *74*, 291–305. [CrossRef]
67. Li, Y.; Zhou, X.; Huang, T.; Tian, J.; He, M.; Zhu, X.; Li, J.; Zhang, Y.; Wu, Z.; Li, B. Origins of volatiles and helium fluxes from hydrothermal systems in the Eastern Himalayan Syntaxis and constraints on regional heat and tectonic activities. *J. Hydrol.* **2024**, *631*, 130776. [CrossRef]
68. Wakita, H. Water wells as possible indicators of tectonic strain. *Science* **1975**, *189*, 553–555. [CrossRef]
69. Zhou, X.; Liu, L.; Chen, Z.; Cui, Y.; Du, J. Gas geochemistry of the hot spring in the Litang fault zone, Southeast Tibetan Plateau. *Appl. Geochem.* **2017**, *79*, 17–26. [CrossRef]
70. Sano, Y.; Marty, B. Origin of carbon in fumarolic gas from island arcs. *Chem. Geol.* **1995**, *119*, 265–274. [CrossRef]
71. Ray, M.C.; Hilton, D.R.; Muñoz, J.; Fischer, T.P.; Shaw, A.M. The effects of volatile recycling, degassing and crustal contamination on the helium and carbon geochemistry of hydrothermal fluids from the Southern Volcanic Zone of Chile. *Chem. Geol.* **2009**, *266*, 38–49. [CrossRef]
72. Ford, D.; Williams, P.D. *Karst Hydrogeology and Geomorphology*; John Wiley & Sons: Hoboken, NJ, USA, 2007.
73. Hosono, T.; Masaki, Y. Post-seismic hydrochemical changes in regional groundwater flow systems in response to the 2016 Mw 7.0 Kumamoto earthquake. *J. Hydrol.* **2020**, *580*, 124340. [CrossRef]
74. Shi, Z.; Wang, G.; Liu, C. Advances in research on earthquake fluids hydrogeology in China: A review. *Earthq. Sci.* **2013**, *26*, 415–425. [CrossRef]
75. Tsunogai, U.; Wakita, H. Precursory chemical changes in ground water: Kobe earthquake, Japan. *Science* **1995**, *269*, 61–63. [CrossRef]

76. Shi, Z.; Zhang, H.; Wang, G. Groundwater trace elements change induced by M5.0 earthquake in Yunnan. *J. Hydrol.* **2020**, *581*, 124424. [CrossRef]
77. Xiang, Y.; Peng, S. Hydrochemical and stable isotopes (δ^2H and δ^{18}O) changes of groundwater from a spring induced by local earthquakes, Northwest China. *Front. Earth Sci.* **2023**, *10*, 1100068. [CrossRef]
78. Kumar, S.; Manga, M.; Nair, A.M.; Dixit, A.; Mahanta, C. Water geochemistry and stable isotope changes record groundwater mixing after a regional earthquake in Northeast India. *Geochem. Geophys. Geosyst.* **2024**, *25*, e2024GC011476. [CrossRef]
79. Ding, Z.; Zhou, X.; Wang, C.; Li, J.; He, M.; Tian, J.; Saimaiernaji, K.; Zhu, C.; Yan, W.; Ma, R. Hydrogeochemical characterization and precursor anomalies of hot springs in the North Tianshan orogen. *Appl. Geochem.* **2023**, *158*, 105813. [CrossRef]
80. Li, K.; Li, L.; Aubaud, C.; Muehlenbachs, K. Efficient carbon recycling at the Central-Northern Lesser Antilles Arc: Implications to deep carbon recycling in global subduction zones. *Geophys. Res. Lett.* **2020**, *47*, e2020GL086950. [CrossRef]
81. Dasgupta, R.; Hirschmann, M.M. The deep carbon cycle and melting in Earth's interior. *Earth Planet. Sci. Lett.* **2010**, *298*, 1–13. [CrossRef]
82. Mörner, N.-A.; Etiope, G. Carbon degassing from the lithosphere. *Glob. Planet. Change* **2002**, *33*, 185–203. [CrossRef]
83. Van Soest, M.; Hilton, D.; Kreulen, R. Tracing crustal and slab contributions to arc magmatism in the Lesser Antilles island arc using helium and carbon relationships in geothermal fluids. *Geochim. Cosmochim. Acta* **1998**, *62*, 3323–3335. [CrossRef]
84. Sabine, C.L.; Heimann, M.; Artaxo, P.; Bakker, D.C.; Chen, C.-T.A.; Field, C.B.; Gruber, N.; Le Quéré, C.; Prinn, R.G.; Richey, J.E. Current status and past trends of the global carbon cycle. *Scope-Sci. Comm. Probl. Environ. Int. Counc. Sci. Unions* **2004**, *62*, 17–44.
85. Barberio, M.D.; Barbieri, M.; Billi, A.; Doglioni, C.; Petitta, M. Hydrogeochemical changes before and during the 2016 Amatrice-Norcia seismic sequence (central Italy). *Sci. Rep.* **2017**, *7*, 11735. [CrossRef]
86. Skelton, A.; Andrén, M.; Kristmannsdóttir, H.; Stockmann, G.; Mörth, C.-M.; Sveinbjörnsdóttir, Á.; Jónsson, S.; Sturkell, E.; Guðrúnardóttir, H.R.; Hjartarson, H. Changes in groundwater chemistry before two consecutive earthquakes in Iceland. *Nat. Geosci.* **2014**, *7*, 752–756. [CrossRef]
87. Zhao, Y.; Liu, Z.; Li, Y.; Hu, L.; Chen, Z.; Sun, F.; Lu, C. A case study of 10 years groundwater radon monitoring along the eastern margin of the Tibetan Plateau and in its adjacent regions: Implications for earthquake surveillance. *Appl. Geochem.* **2021**, *131*, 105014. [CrossRef]
88. Zheng, G.; Wang, H.; Wright, T.J.; Lou, Y.; Zhang, R.; Zhang, W.; Shi, C.; Huang, J.; Wei, N. Crustal deformation in the India-Eurasia collision zone from 25 years of GPS measurements. *J. Geophys. Res. Solid Earth* **2017**, *122*, 9290–9312. [CrossRef]